Performance investigation of liquid-solid heat transfer from 177 to 95 K in moving solid-phase cold storage

Yihong Li[1, 2], Xiaoyu Fan[1, 2], Junxian Li[1, 2], Zhikang Wang[1, 2], Jiamin Du[1, 2], Zhaozhao Gao[1, 4], Wei Ji[3, *], Guoyao Yu[1], Liubiao Chen[1, 2, 4, *] and Junjie Wang[1, 2, 3]

[1] State Key Laboratory of Cryogenic Science and Technology, Technical Institute of Physics and Chemistry, Chinese Academy of Sciences, Beijing, China
[2] University of Chinese Academy of Sciences, Beijing, China
[3] Zhonglv Zhongke Energy Storage Technology Co., Ltd., Beijing, China
[4] Institute of Optical Physics and Engineering Technology, Qilu Zhongke, Jinan, China

[*]E-mail: ji-wei@cgdg.com
chenliubiao@mail.ipc.ac.cn

Abstract. Liquid air energy storage (LAES) is an emerging energy storage technology characterized by its high energy density and non-polluting nature. It stores surplus electricity through the processes of compression, cooling, and liquefaction of air, and releases electricity to compensate grid loads through the pressurization, gasification, and expansion of liquid air. The core process involves the storage of cold energy from air liquefaction and gasification. Due to the inherent safety and low material costs, solid-phase cold storage technology has been widely studied. Among these technologies, the fixed particle packed bed cold storage technology is the most extensively researched, but it suffers from dynamic effects due to thermocline development during heat transfer, limiting efficiency improvements. Based on this research status, we propose a moving solid-phase cold storage process where the cold storage particles exchange heat with the carrier liquid in a counter-current flow and store the cold and heat particles separately. The movement of particles can mitigate the adverse effects of the thermocline, thereby enhancing heat transfer efficiency. In this study, we construct a model of the heat transfer process and investigate the matching characteristics of liquid-solid phase velocities as well as the establishment of a steady-state heat transfer process.

1. Introduction

The global transition toward energy decarbonization has driven sustained growth in renewable power generation [1]. However, the integration of renewable energy into power grids presents significant challenges due to its inherent intermittency, raising concerns about system stability [2]. Additionally, temporal disparities in grid power demand have created nighttime energy surpluses and daytime power deficits. These challenges have accelerated the development of large-scale energy storage technologies capable of stabilizing grid fluctuations and facilitating peak load management [2].

Liquid air energy storage (LAES) has emerged as a promising solution among large-scale energy storage technologies, distinguished by its high energy density and location flexibility [3]. The system operates through two phases [3]: an energy charging phase involving air compression, cooling, and liquefaction, and an energy discharging phase comprising liquid air regasification, rewarming, and expansion. The system's efficiency fundamentally depends on its cold energy storage mechanism, where thermal energy recovered during air regasification is stored for subsequent use in air pre-cooling during charging phases.

Contemporary LAES systems utilize two primary cold storage methods [4]: liquid-phase thermal storage and solid-phase packed-bed thermal storage. Liquid-phase systems employ organic fluids as both storage media and heat transfer fluids (HTFs) for air heat exchange. Solid-phase systems utilize granular materials such as rocks and glass beads for storage, with gaseous HTFs (typically nitrogen) facilitating thermal energy transfer between air and packed beds. While solid-phase systems offer advantages in cost and safety through non-flammable materials, their efficiency is compromised by thermocline migration during cyclic operation [4]. Conversely, liquid-phase systems achieve higher efficiency but require substantial quantities of expensive, potentially hazardous organic HTFs [4].

This research presents an innovative liquid-solid cold storage solution to address these limitations: a continuously moving packed-bed system where solid particles ascend at constant velocity through a chain-baffles structure. This configuration enables counter-current heat exchange between rising particles flow and descending liquid HTF, establishing steady-state thermal transport. The design offers several advantages: (1) enhanced cold storage efficiency through elimination of thermocline dynamics, (2) reduced hazardous liquid HTF requirements while maintaining solid-phase media cost benefits, and (3) stable heat transfer process achievement. This study examines the establishment of steady-state heat transfer conditions and velocity-matching characteristics between liquid HTF and solid particles.

2. System layout

As shown in Figure 1(a), a conventional LAES system consists of four main components: multistage compressors, a dual-stage cold storage subsystem with heat exchangers, an air liquefaction unit with tank, and multistage expanders. In the charging phase, ambient air undergoes multistage compression with interstage cooling by thermal oil, reaching high-pressure ambient-temperature conditions. The compressed air then cools to liquefaction temperatures through the cold storage subsystem, followed by depressurization via a cryogenic turbine. A portion of un-liquefied air circulates back to precool incoming airflow, while the remainder undergoes liquefaction and storage in a liquid air tank, completing the energy storage cycle. During discharge, cryogenic liquid air is pressurized using cryogenic pumps before undergoing cold energy recovery in dual-stage heat exchangers. The re-gasified air warms to ambient temperature and subsequently absorbs stored compression heat from thermal oil to power multi-stage expanders for electricity generation.

This research introduces a novel liquid-solid cold storage system utilizing organic fluids as the heat transfer fluid (HTF), as shown in Figure 1(b). The system comprises a vertical channel integrated with a chain-driven baffle structure, which facilitates the upward transport of solid particles at a constant velocity between hot and cold storage tanks. Strategically positioned weep holes on the baffles and along the vertical channel permit the downward flow of the HTF, establishing a counter-current heat exchange with the upward-moving particles. The liquid-phase HTF is propane, an organic compound commonly adopted in the second-stage cold storage of

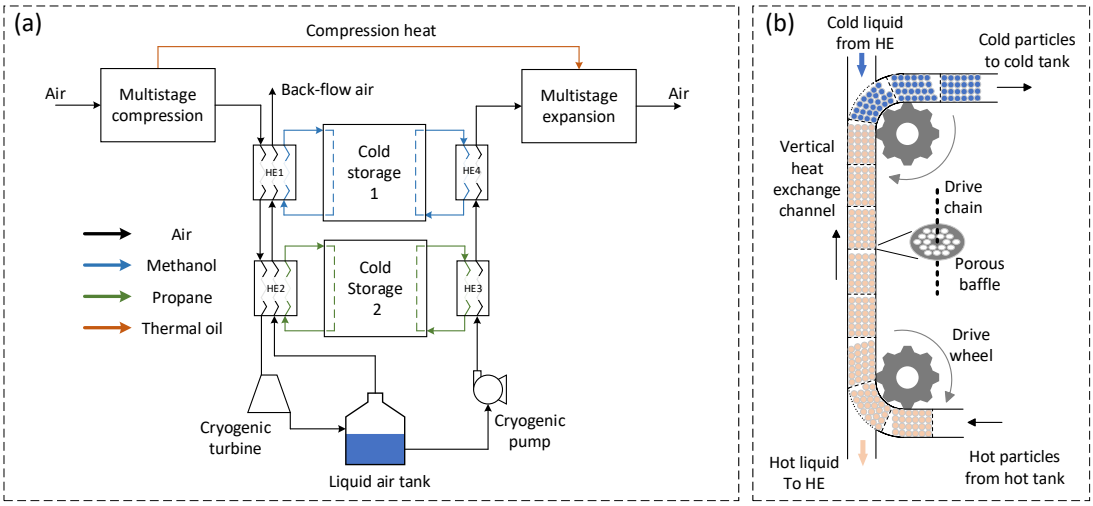

Figure 1. Layout of LAES system (a) and liquid-solid cold storage (b).

liquid air energy storage (LAES) systems [2]. The solid phase consists of glass beads, selected for their spherical morphology to promote efficient transport. Both materials operate within a temperature range of 95–177 K.

The cold storage process utilizing propane and glass beads is described as follows: Cold propane from HE3 (Figure 1(a)), having recovered cold energy from the air, enters the apex of the vertical channel and engages in counter-current heat exchange with the ascending warm glass beads. The subsequently heated propane returns to HE3 for further cold energy recovery from the air, while the cooled glass beads are transported into the cold tank for cold energy storage. System mode switching (between cold storage and release) is achieved through synchronized control of the inlet and outlet valves on the cold and hot tanks. This study focuses on the liquid-solid heat transfer characteristics during the cold storage process within the vertical heat exchange channel, as well as the velocity-matching behaviour between the propane HTF and glass bead flows.

3. Modelling and evaluation of heat transfer

3.1 Assumptions and modelling

This investigation examines the counter-current heat exchange process between upward-moving glass beads and downward-flowing liquid propane within the vertical channel. Numerical simulations were performed using ANSYS FLUENT under the following assumptions:

1. Constant upward velocity of glass beads imposed by drive wheels;
2. Ignore the volume occupied by chains and baffles;
3. Adiabatic boundary conditions for channel wall;
4. Monodisperse glass bead diameter distribution with 5 mm;
5. Temperature-dependent thermophysical properties for both glass beads and propane;
6. Eulerian-Eulerian two-phase model treating glass beads as a virtual fluid phase;
7. Initial conditions with cryogenic propane and hot glass beads filling the channel.

The rationale for employing the Eulerian–Eulerian two-phase model, wherein the glass beads are treated as a virtual fluid, originates from Fan et al. [5]. This approach was adopted to efficiently analyze the temperature distribution of both the glass beads and the fluid within the flow field. In contrast, the dense discrete particle model (DDPM) necessitates the computation of temperature variations, momentum equations, and trajectory tracking for each individual bead. Consequently, the DDPM is considerably more computationally expensive and slower than the Eulerian–Eulerian model. Therefore, the Eulerian–Eulerian framework was selected for this study. Essential simulation parameters are summarized in Table 1. The thermophysical properties of glass beads were obtained from Fan et al. [5], while propane properties were extracted from the NIST

REFPROP database. The glass bead velocity was established through consultations with transportation device manufacturers, selecting conservative values to ensure operational feasibility. Propane velocity was calculated based on thermal capacity matching (detailed in section 3.3), with corresponding Reynolds numbers (Re) indicating laminar flow. The Gunn correlation [6], validated for heat transfer between particles-flow and fluid, was implemented. A 1 m high and 0.15 m width vertical channel was discretized using 2D structured meshes with a 12.5 mm mesh size, achieving a balance between computational efficiency and resolution accuracy.

Table 1. Key parameters in simulating liquid-particles heat transfer.

Parameters	Value
Density (ρ_p), specific heat ($C_{P,p}$), thermal conductivity (λ_p) of glass beads	Fan et al. [5]
Diameter of glass beads, d_p	5 mm [5]
Porosity of glass beads bed, ε	0.4 [5]
Conveying velocity of glass beads, V_p	0.02 m/s
Density (ρ_l), specific heat ($C_{P,l}$), thermal conductivity (λ_l) and dynamic viscosity (μ_l) of 0.1MPa propane	From NIST
Operating temperature range of heat transfer	177-95 K [7]
Flow regime of propane	Laminar
Liquid-particles heat transfer correlation	Gunn [6]
Channel length	1 m
Channel diameter	0.15 m
Mesh size (2D structured mesh)	12.5 mm
Granular viscosity	gidaspow
Granular bulk viscosity	lun-et-al
Packing limit	0.63
CFL number	0.016-0.024
Time step size	0.008 s
Spatial discretization of momentum and energy	Second order upwind
Relaxation factors for momentum and energy	0.5

3.2 Mesh size verification

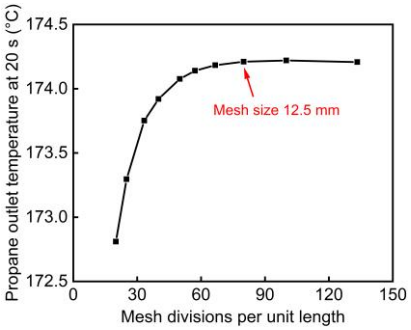

Figure 2. Mesh size verification.

To ensure that the simulation results are independent of the mesh size, a mesh independence study was conducted. The validation approach involved comparing the propane outlet temperature at a physical time of 20 s across simulations with different mesh resolutions. As shown in Figure 2, the propane outlet temperature gradually increased with finer meshing and eventually converged to a stable value. A mesh size of 12.5 mm (80 divisions per unit length) was selected to ensure mesh-independent results while maintaining computational efficiency.

3.3 Evaluation of heat transfer

This study examines counter-current liquid-particles heat transfer under an Eulerian-Eulerian framework, necessitating a prior determination of phase velocity. The particles' velocity was fixed at 0.02 m/s, while the liquid velocity was derived from thermal equilibrium considerations (Equation 1):

$$\rho_p V_p (1-\varepsilon) \int_{95}^{177} C_{P,p}\, \mathrm{d}T = \rho_l V_l \varepsilon \int_{95}^{177} C_{P,l}\, \mathrm{d}T \tag{1}$$

where subscripts *p* and *l* denote particles and liquid phases, respectively. This equation assumes near-zero temperature differences at both channel ends — a hypothesis validated in subsequent results (section 4.1). Temperature-dependent heat capacities were obtained from NIST (propane) and literature data (glass beads), with liquid density and velocity evaluated at the 177 K bottom outlet.

Following velocity determination, the interphase heat transfer model was specified. The Gunn correlation (Equation 2 to Equation 5) was selected for its validated applicability to systems with porosity $0.35 \le \varepsilon \le 1.0$ and Re number up to 10^5. The counter-flow configuration requires relative velocity $|V_p - V_l|$ for Re number calculation (relative/slip Re, noted as Re_s) and flow regime assessment. At the calculated liquid velocity (Equation 1) and 177 K conditions, $Re_s \approx 416$ confirmed laminar dominance. Gunn correlation [6]:

$$N_u = (7 - 10\varepsilon + 5\varepsilon^2)\left(1 + 0.7 Re_s^{0.2} P_r^{\frac{1}{3}}\right) + (1.33 - 2.4\varepsilon + 1.2\varepsilon^2)\, Re_s^{0.7}\, P_r^{\frac{1}{3}} \tag{2}$$

$$Re_s = \frac{|V_p - V_l| \rho_l\, \mathrm{d}_p}{\mu_l} \tag{3}$$

$$P_r = \frac{C_{P,l}\mu_l}{\lambda_l} \tag{4}$$

$$h = \frac{\lambda_l N_u}{d_p} \tag{5}$$

Under the adiabatic boundary assumption, thermal efficiency analysis was omitted. Exergy analysis was not included due to page limitations. The logarithmic mean temperature difference (LMTD) was considered unsuitable due to asymptotic temperature convergence at one channel end. The analysis focused on axial temperature distributions, local temperature differences ($\Delta T = T_p - T_l$), and average temperature difference (ΔT_{ave} in Equation 6).

$$\Delta T_{ave} = \frac{1}{L}\int_0^L \Delta T\, \mathrm{d}L \tag{6}$$

4. Results and discussion

4.1 Establishment of steady-state heat transfer

At a fixed particles' velocity *Vp*=0.02 m/s, Equation 1 yields a liquid propane outlet velocity *Vl*=−0.03227 m/s (negative sign indicating counter-flow direction). The temporal evolution of

phase outlet temperatures and axial temperature profiles are presented in Figure 3(a) and 3(b), respectively. Figure 3(a) demonstrates rapid thermal equilibration: the cold propane outlet temperature increases to 176.2 K at t=60 s, while the hot particles outlet temperature decreases to 96.6 K. The remaining temperature differentials resolve gradually, reaching near-steady states at t=800 s, with temperatures of 176.996 K for liquid and 95.033 K for particles (ΔT<0.01 K compared to stabilized). The minimal difference between the stabilized liquid temperature and the initial assumption (177 K) for liquid velocity eliminates the necessity for iterative liquid velocity refinement.

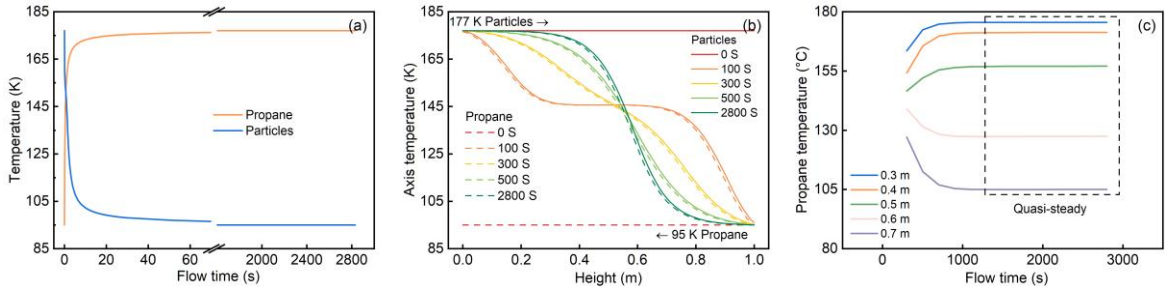

Figure 3. Changes in outlet temperatures (a), axial temperature distribution (b), and propane temperature at different height (c).

However, outlet temperature stabilization does not necessarily indicate global steady-state conditions. Figure 3(b) illustrates the progressive axial thermal development: The initial conditions (t=0 s) exhibit uniform temperatures of 95 K (liquid) and 177 K (particles). At t=100 s, thermal gradients emerge within 0.3 m regions near both ends, surrounding a 0.4 m isothermal zone in the middle section. This transitional configuration dissipates by t=300 s, resulting in continuous gradients throughout the channel. Significantly, the continued gradient migration leads to quasi-steady distributions at t≈2800 s, with primary temperature differentials concentrated between 0.3-0.8 m heights and minimal temperature variations in the end zones. To further characterize this quasi-steady regime, Figure 3(c) presents the temporal evolution of propane temperature at selected axial heights. The rate of temperature change at each location decreases over time, becoming negligible after approximately 1200 s, thereby confirming the establishment of a quasi-steady state.

4.2 Effect of propane velocity deviation

Building upon the stabilized temperature profiles established in section 4.1 (V_p=0.02 m/s, V_l=−0.03227 m/s), this section analyzes the thermal response under liquid velocity variations (±20 %, ±10 %). Figure 4(a)-(c) illustrate the quasi-steady-state temperature distributions, ΔT distribution, and velocity-dependent ΔT value changing trends, respectively.

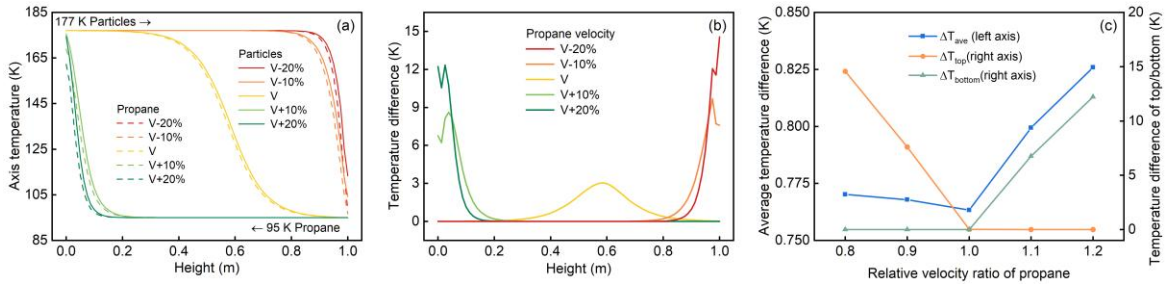

Figure 4. Temperature distribution (a), ΔT distribution (b), and ΔT magnitude (c) under different propane velocity deviation.

The temperature distribution shifts (Figure 4(a)), as liquid velocity variations influence the heat transfer and balance. Lower velocities cause the primary heat exchange zones to concentrate near the channel top (liquid inlet), while higher velocities shift these zones toward the bottom (liquid outlet). Additionally, the intensity of thermal gradients increases positively correlated with the magnitude of velocity deviation.

The ΔT distribution changes with velocities (Figure 4(b)): at matched velocities, temperature differences (ΔT) exhibit a near-Gaussian distribution (peak ~3 K) between 0.3–0.8 m. Velocity deviations alter this profile: a +20 % deviation concentrates ΔT near the bottom (0-0.15 m, ΔT_{max}=12.34 K), while a -20 % deviation shifts peaks toward the top (0.85-1 m, ΔT_{max}=14.56 K). The occurrence of local ΔT minima may be attributed to non-uniform trends in temperature-dependent properties between phases.

The ΔT values vary with velocity (Figure 4(c)), as velocity modifications alter the ΔT distribution and mean temperature difference (ΔT_{ave}). The ΔT_{ave} reaches its minimum at 0.763 K under velocity-matching conditions. Velocity deviation-induced increases demonstrate asymmetry: a +20 % velocity results in 8.3 % higher ΔT (0.826 K), while a -20 % deviation produces a 1.0 % increase (0.770 K). This asymmetry results from residence time effects: higher velocities reduce fluid-particles contact time despite enhanced convection, significantly increasing ΔT; conversely, velocity reduction weakens heat transfer, but the extended residence time produces only a minimal increase in ΔT_{ave}. Furthermore, increased liquid velocity amplifies ΔT_{bottom} (15 K at +20 %) while maintaining ΔT_{top} near 0 K, whereas decreased velocity elevates ΔT_{top} while preserving ΔT_{bottom}.

4.3 Effect of particles velocity deviation

Figure 5 depicts the influence of particles velocity variations on temperature distributions, ΔT distributions, and ΔT evolution within the heat exchange channel. The observed trends demonstrate notable symmetry with liquid velocity deviations analysed in section 4.2, though with directional inversion due to opposing inlet configurations.

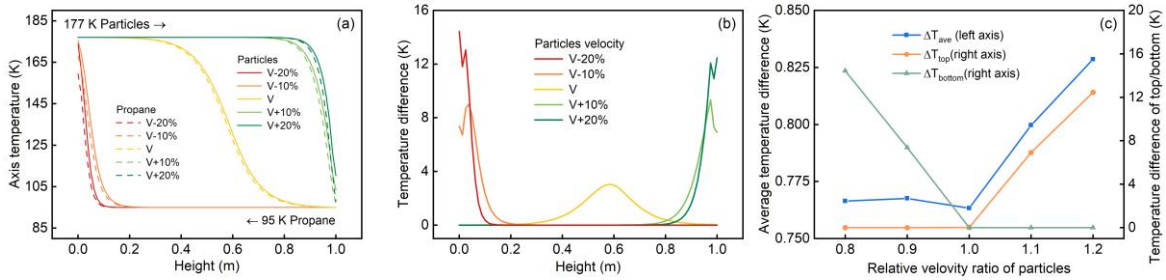

Figure 5. Temperature distribution (a), ΔT distribution (b), and ΔT magnitude (c) under different particles velocity deviation.

The temperature profile exhibits symmetry (Figure 5(a)), where decreased particles velocities enhance thermal gradients while shifting primary heat transfer regions toward the channel bottom (particles inlet), reflecting an inverted pattern of the liquid velocity deviations. This spatial inversion results from the opposing inlet configurations: liquid enters from the top, while particles enter from the bottom.

The ΔT response patterns (Figure 5(b) and (c)) demonstrate parallel behavior with the results presented in section 4.2. Velocity reductions concentrate temperature differentials near their respective inlets (bottom for particles, top for liquid). The asymmetric escalation in

ΔT_{ave} magnitudes persists: a 20 % reduction in particles' velocity results in ΔT_{ave} =0.766 K, compared to 0.8285 K for a 20 % increase in particles' velocity.

This symmetrical response originates from the Eulerian-Eulerian two-fluid framework's treatment of phase equivalence, wherein both phases are modelled as interpenetrating continua governed by analogous conservation laws. This mathematical isomorphism naturally generates mirrored thermal responses to velocity perturbations.

5. Conclusion

This study examines counter-current heat transfer in a novel liquid-solid cold storage system for LAES, emphasizing the quasi-steady-state establishment and velocity-dependent thermal interactions between glass beads and liquid propane. The key findings are summarized as follows:

1. Dynamic-to-steady-state transition: under initial conditions with cryogenic propane (95 K) and hot glass beads (177 K) filling the channel, near-thermal equilibrium at phase outlets is achieved within 60 s. However, global steady-state temperature distribution across the entire channel requires over 2000 s to establish. Quasi-steady end temperature differentials remain below 0.1 K under thermal capacity matching conditions.
2. Velocity matching characteristics: at matched velocities (V_p=0.02 m/s, V_l=0.03227 m/s), the system minimizes the mean temperature difference (ΔT_{ave}=0.763 K) with near-zero outlet discrepancies. Velocity deviations (±20 %) asymmetrically perturb equilibrium, increasing ΔT_{ave} to 0.826 K (+20 %) but 0.770 K (-20 %).
3. Symmetric thermal response: phase velocity deviations produce mirror-imaged spatial shifts in thermal gradients and ΔT distributions. Reduced particles' velocities (V_p<0.02 m/s) relocate dominant heat transfer zones toward the channel bottom (particles inlet), whereas reduced liquid velocities (V_l<0.03227 m/s) shift gradients upward (liquid inlet). This directional inversion results from opposing inlet configurations.

Acknowledgments

This work is supported by the National Key Research and Development Program of China (2024YFE0208500), the Postdoctoral Fellowship Program of CPSF (GZC20241778), and technological innovation projects of China Green Development Investment Group Co., Ltd. (No. 09CHDD020 and No. 09CHDD021).

References

[1] Nassar Y, El-Khozondar H and Fakher M. 2025 Journal of Energy Storage. **108** 115224.
[2] She X, Wang H, Zhang T, et al. 2025 Renewable and Sustainable Energy Reviews. **208** 114986.
[3] Agyekum E and Odoi-Yorke F. 2024 Journal of Energy Storage. **102** Nov. Pt. A.
[4] Ding X, Duan L, Zheng N, et al. 2025 Renewable and Sustainable Energy Reviews. **210** 115164.
[5] Fan X, Xu H, Li Y, et al. 2024 Applied Energy. **371** 123739.
[6] Gunn D. 1978 Int. J. Heat Mass Transfer. **467-476** Vol. 21.
[7] Li Y, Fan X, Li J, et al. 2024 Applied Thermal Engineering. **245** 122909.